

Study of vortical separation from an axisymmetric hill

Roger L. Simpson ^{*}, C.H. Long, G. Byun

Department of Aerospace and Ocean Engineering, Virginia Polytechnic Institute and State University, Blacksburg, VA 24061-0203, USA

Abstract

Surface mean pressures, oil-flow visualizations, and three-velocity-component laser-Doppler velocimeter measurements are presented for a turbulent boundary layer of thickness δ over an axisymmetric hill of height $H = 2\delta$. Complex vortical separations occur on the leeside and merge into two large streamwise mean vortices downstream. At $x/H = 3.69$, the near-wall flow ($y^+ < 90$) is dominated by the wall, while the vortices in the outer region produce large turbulence levels near the centerline and appear to have low frequency motions that contribute to turbulent diffusion. © 2002 Elsevier Science Inc. All rights reserved.

1. Introduction

There have been a few previous studies of boundary layer flow over an axisymmetric hill, although little has been reported about the near-wall and separated vortical flows in references cited by Ishihara et al. (1999). Ishihara et al. examined the flow in the center plane of an axisymmetric hill that had a cosine-squared cross section and a maximum slope of 32° . The approach boundary layer thickness δ to hill height H ratio was 9 and the Reynolds number $U_H H/\nu = 1.1 \times 10^4$, where U_H is the velocity at the height H for the undisturbed boundary layer. Although little was presented about the flow away from the center plane, it was clear that the flow accelerated over the top and around the sides of the hill. A leeside separation and a reattachment at the foot of the hill occurred with low frequency motions ($0.065 < fH/U_H < 0.13$) in the downstream wall layer at $x/H = 3.75$.

Some objectives of the current research program are to measure and understand the formation and structure of vortical 3D turbulent separations of a turbulent boundary layer over axisymmetric hills or bumps, which are used to create strong streamwise vortices that energize the downstream boundary layer. Of particular interest are data that describe the turbulent diffusion processes that control the momentum transfer rates that affect the vortical separation. Another objective is to provide test cases to compare with and modify turbu-

lence models that are used to calculate such flows. Axisymmetric hills were selected which have multiple separations over a large area of the leeside. Such flows are more demanding of turbulence models than attached or massively separated flow cases.

In order to understand the nearest wall flow where the separations originate, detailed surface pressure distributions and surface oil-flow patterns were obtained. Precise very near-wall measurements of mean velocities, turbulent stresses, triple products and skin friction are being obtained. The results for only one bump with $\delta/H = 1/2$ are presented here.

2. Experimental apparatus and flow conditions

The measurements were conducted in the VPI&SU AOE Dept. Low Speed Boundary Layer Wind Tunnel, which has been used in much previous work and is described by Devenport and Simpson (1990). At a nominal speed of $U_{\text{ref}} = 27.5$ m/s, temperature of (25 ± 1) °C, the turbulence intensity observed in the tunnel freestream was 0.1% and the potential core was uniform to within 0.5% in the spanwise and 1% in the vertical directions. When the bump was not in place, a mean 2D zero pressure gradient turbulent boundary layer 39 mm thick was present with $Re_\theta = 7300$, which are the same conditions reported by Ölçmen and Simpson (1995).

The bump was mounted in the center floor of the 0.91 m wide, 0.25 m high, and 7.62 m long test section 3.03 m from the test section leading edge. It was machined from wood with the shape shown in Fig. 1 that is defined by

^{*} Corresponding author.

E-mail address: simpson@aoe.vt.edu (R.L. Simpson).

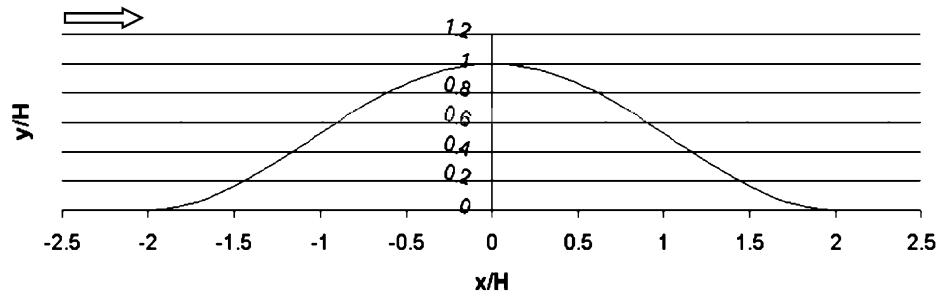


Fig. 1. Shape of the axisymmetric hill.

$$\frac{y(r)}{H} = -\frac{1}{6.04844} \left[J_0(A) I_0\left(A \frac{r}{a}\right) - I_0(A) J_0\left(A \frac{r}{a}\right) \right],$$

where $A = 3.1926$, $H = 78$ mm is the height of the bump, and $a = 2H$ is the radius of the circular base of the bump. J_0 is the Bessel function of the first kind and I_0 is modified Bessel function of the first kind. To avoid warping, the bump was painted black and coated with a clear sealer. The Reynolds number based on the height H and U_{ref} is $Re_H \approx 1.3 \times 10^5$.

3. Laser-Doppler system

Two configurations of a three-orthogonal-velocity-component fiber-optic LDV system were used to obtain coincident instantaneous U , V and W components of the velocity through the transparent glass test wall. In the nearer wall LDV configuration, which is well described by Ölçmen and Simpson (1995) including velocity measurement uncertainties, measurements can be made within 40 mm of the surface; the effective measurement volume of approximately 30 μm in diameter permits precise near-wall (about $y^+ = 3$) measurements. In the outer layer LDV configuration, which is well described by Ölçmen et al. (2001) including velocity measurement uncertainties, measurements can be made within 161 mm of the surface with a reduced spatial resolution of 88 μm , which is of no consequence for outer layer spatial resolution. The data validation percentage from the Macrodyne Model 3100 Frequency Domain Processors was above 98%, which resulted in minimally noisy data. One block of 30 000 samples over several minutes was taken for each measurement point. The aerosol seeding system (Ölçmen and Simpson, 1995) used dioctyl phthalate (DOP) with a measured mean particle size of about 2 μm . The outlying data points from histograms were removed in the LDV optics co-ordinate system as well as after rotation into the tunnel co-ordinate system, as described by Ölçmen and Simpson (1995). Since there was no correlation between the data rate fluctuation and the velocity magnitude fluctuation, no velocity bias correction was applied. Velocity gradient, finite transitive, and instrument broadening of the signals were also

negligible (Long, 2002). The data shown here are a composite of data from the two LDV configurations.

As described by Long, when the measurement volume was focused just onto the surface, a strong signal determined an approximate reference location for a LDV traverse. A more refined determination of the measurement volume location relative to the wall was obtained by a least squares curve fit of the viscous sublayer mean velocity profile, $Q = C_1 y + C_2 y^4$, with $Q = (U^2 + W^2)^{1/2}$ and C_1 and C_2 as coefficients. The curve was fit through $Q = 0$ at $y = 0$. Using only the data for $y^+ < 10$, an iterative process was used to maximize the curve fit correlation coefficient by shifting the y values by Δy . This was performed at each of the profiles using at least five points. Most of the optimum Δy shifts were less than 50 μm . Using this curve fit, the wall shearing stress $\tau_w/\rho = \nu(\partial Q/\partial y)_{\text{wall}} = U_\tau^2 = C_1 \nu$.

4. Surface static pressure coefficient and vorticity flux

Mean static pressure distributions were measured on the surface of the bump and the plate upstream and downstream by using multiple pressure taps flush with the surface that are connected to a Scani-valve system. The static pressure coefficient C_p is calculated as $(p_{\text{local,static}} - p_{\text{ref,static}})/(p_{\text{ref,total}} - p_{\text{ref,static}})$, where $p_{\text{ref,static}}$ and $p_{\text{ref,total}}$ are the static and stagnation pressures of the undisturbed freestream that determine U_{ref} and are measured by a Pitot-static tube mounted 1.4 m upstream of the center of the bump, where $X = 0$. The 0.5 mm diameter pressure taps were placed along a radial line of the bump 6.35 mm apart. The pressure measurements were made at every 10° of peripheral angle by turning the bump around the y -axis of symmetry. Three dozen pressure taps were placed on the flat Plexiglas plate. These pressure taps were only at one side of the centerline, because the flow over the plate is symmetric about the centerline as checked by the pressure data on the bump. Also the taps on the plates were only placed at one side of the bump (upstream or downstream), but the pressure data were taken for both upstream and downstream by turning the plates with the bump 180° .

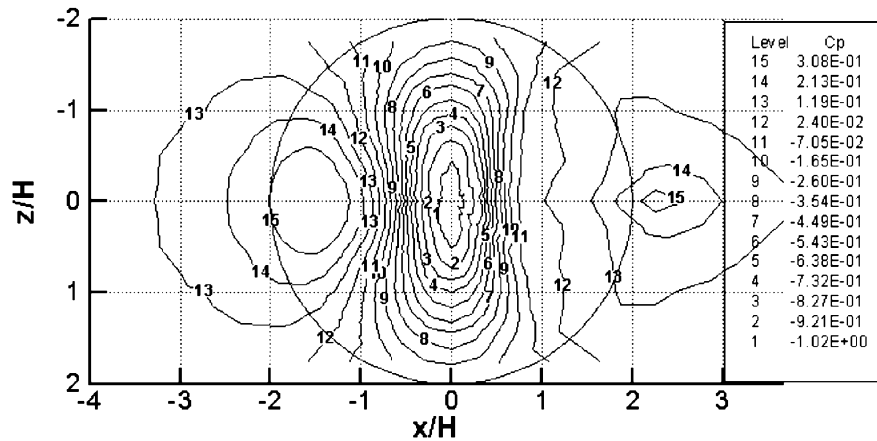


Fig. 2. Contours of interpolated C_p measurements on the hill.

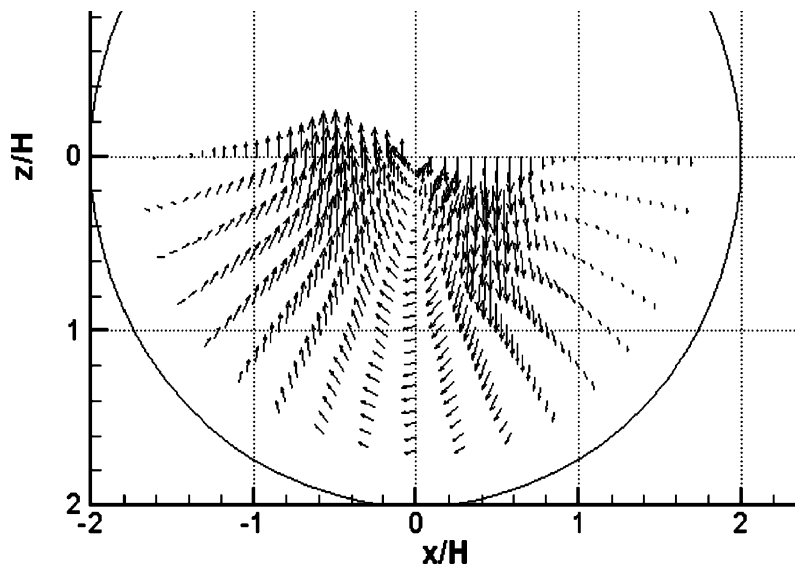


Fig. 3. Vector plot of vorticity flux (relative scale) at surface for half of the bump.

The contour plot of surface static pressure coefficient C_p (± 0.02 uncertain) is shown in Fig. 2, which uses data from both sides of the plane of symmetry. Differences of C_p are generally less than ± 0.02 from an average for any two symmetric locations and show good symmetry.

For incompressible flow over stationary surfaces with a unit vector normal to the surface \vec{e}_n , all vorticity $\vec{\omega} = \frac{1}{2} \text{curl} \vec{V}$ arises at the surface under the action of pressure gradients. The flux of vorticity at the surface is directly proportional to and perpendicular to the pressure gradient at the surface

$$\frac{4}{Re_H} \left(\frac{\partial(\vec{\omega}H/U_{\text{ref}})}{\partial(n/H)} \right)_w = -(\vec{e}_n \times \vec{\nabla}) C_p.$$

The vector plot of $-(\vec{e}_n \times \vec{\nabla}) C_p$, which is the non-dimensional vorticity flux, is presented in Fig. 3. The vortex filaments are created in closed loops which coincide with isobars in Fig. 2. The fresh vorticity on the

upstream side of the bump is of the same sign as the approach boundary layer vorticity. On the sides of the bump the new vorticity is mainly in the streamwise direction. Downstream of the bump top, the fresh vorticity is opposite to that of the approach boundary layer. The non-uniform generation of vorticity across the flow and the rate of diffusion of vorticity control the 3D separation patterns.

5. Surface oil-flow visualization

Surface oil-flow visualization of skin friction lines, high and low velocity regions, separations and reattachments were obtained for the bump and the tunnel floor. The oil mixture was 20% oleic acid, 20% titanium dioxide, and 60% kerosene. The surface of the black model and the Plexiglas plate that was covered with self-

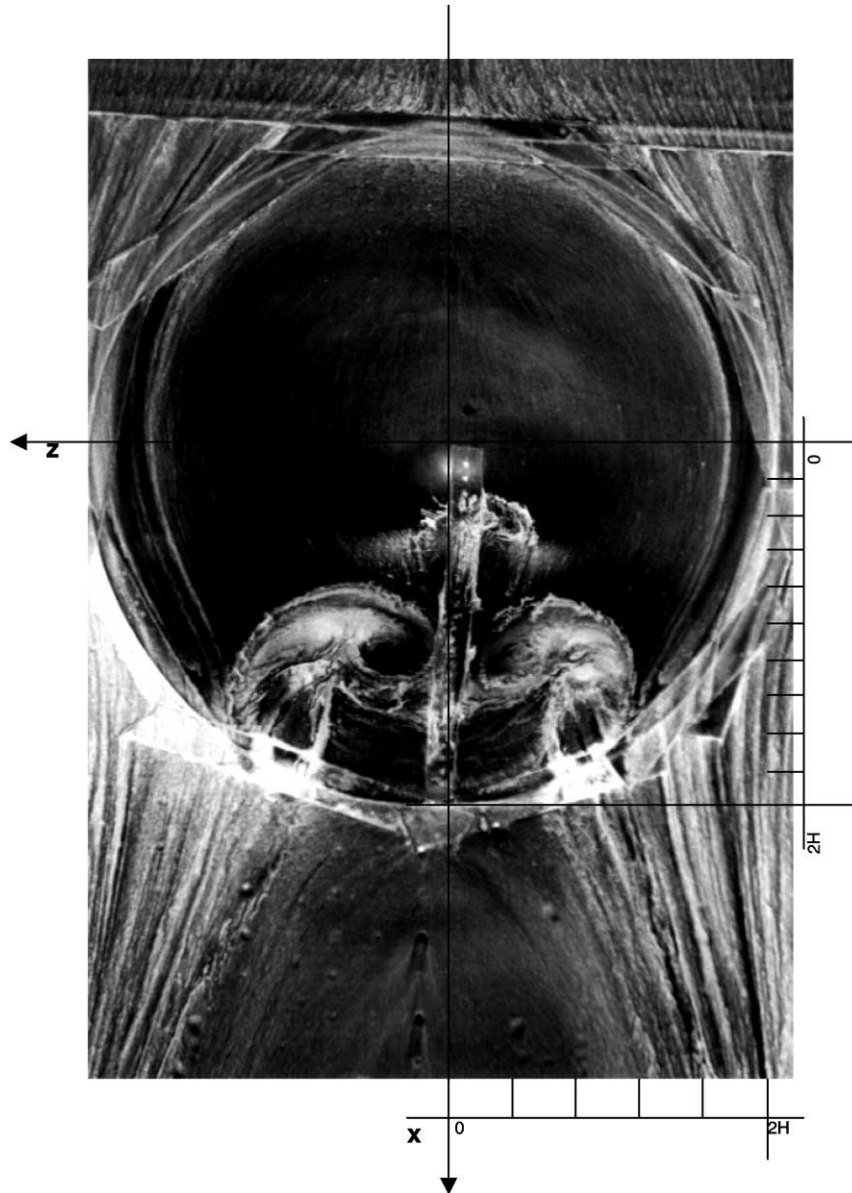


Fig. 4. Perspective topview of an oil flow on the bump. Note some distortion.

adhesive black plastic film were coated uniformly with a layer of the oil mixture. The tunnel was turned on as soon as the oil mixture was applied and kept running until the flow moved the oil into a consistent and partially dry streak. The streaks form wall shear-stress lines, i.e. a limiting streamline pattern. The patterns were photographed, examined and preserved by clear acrylic spray lacquer.

The oil-flow pattern photographed during the flow (Fig. 4) was not definitive in the strong separation region on the leeside of the bump because excessive oil mixture accumulated where the shear-stress lines spiraled into foci and tended to flow down the bump due to gravity. Videos were made to observe movement of the oil mixture; static pictures were made from the video for

further quantitative analysis. Also, small drops of the oil mixture were placed on the leeside of a clean bump and video was taken. This helped to determine definitively the direction of oil-flow movement. The resulting oil-flow shear-stress line pattern was interpreted according to the kinematical topological rules described by Hunt et al. (1977) and is shown in Fig. 5.

6. Discussion of oil-flow visualization and surface static pressure distribution

There is no separation on the front of the bump, but the flow decelerates and oil flow accumulates there. Then the flow accelerates until the top of the bump,

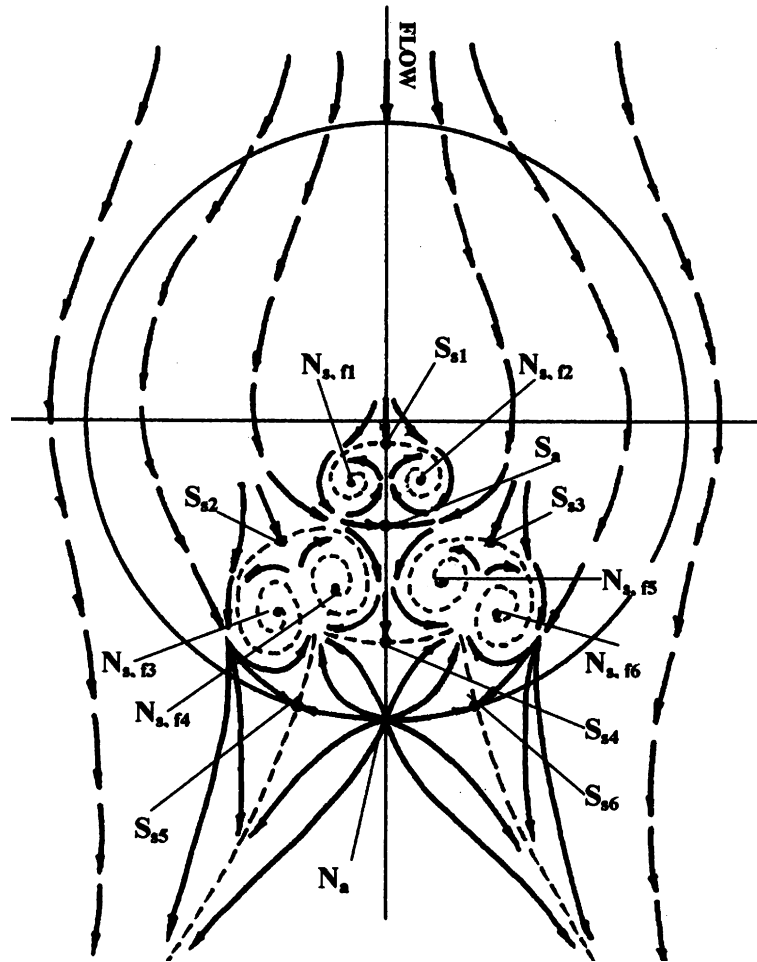


Fig. 5. Shear-stress lines and zero-shear-stress points S and N on the bump surface.

where the oil flow is dark (Fig. 4) since the shearing stress is large and there is little oil mixture left. Downstream on the leeside there is a region with much accumulated oil-flow mixture, approximately from $x/H = 0.18$ to 0.4 and from $z/H = \pm 0.35$. From the shear-stress lines in Fig. 5, there is one saddle separation S_{s1} on the x -axis, followed by symmetrical foci node separations $N_{s, \text{focus1}}$ and $N_{s, \text{focus2}}$ on each side of the centerline. Just downstream a saddle attachment S_a occurs around which the oil flow is darker because of higher shearing stresses. From the C_p (Fig. 2) and pressure gradient (magnitude proportional to vorticity flux in Fig. 3) distributions, we can see that this area is also followed by a region from $x = 0.4H$ to $0.5H$ with very high adverse pressure gradients. A large separation appears to start from this region with a relaxation of the pressure gradients downstream. After $x/H = 0.8$, between $\pm 30^\circ$ of the centerline, the pressure only increases slightly. Saddle separations S_{s2} and S_{s3} occur symmetrically near $x = 0.8H$ and $z = \pm 0.7H$. Foci separations $N_{s, \text{focus3}}$ and $N_{s, \text{focus4}}$ are downstream of S_{s2} and $N_{s, \text{focus5}}$ and $N_{s, \text{focus6}}$ are downstream of S_{s3} , each about $0.4H$ in diameter.

Slightly downstream at about $x = 1.5H$ on the centerline, another saddle separation S_{s4} is located with a distinctly greater accumulation of oil-flow mixture upstream. At the bottom of the bump near $x = 2H$, a nodal attachment N_a occurs, which supplies higher speed fluid in all directions and produces a darker oil flow. Saddle separations S_{s5} and S_{s6} are located on each side of the bottom of the bump at about $z = \pm 0.7H$. Separation lines which pass through S_{s5} and S_{s6} continue downstream and form a line between the higher velocity flow near the centerline and the lower speed flow. The number of saddles and nodes satisfy the topological rule, $\Sigma N = \Sigma S$, which is seven here.

7. LDV results

The LDV results for the undisturbed 2D turbulent boundary layer agreed with previous data and the nearest wall triple products agreed with low Reynolds number DNS results (Long, 2002). The LDV results presented here for the bump were obtained in a $y-z$

plane located at $x/H = 3.69$ downstream from the top of the bump (near the bottom of Fig. 4) with 25 profiles for $0.81 > z/H > -2.85$. The bump spanwise position was adjusted slightly by 2 mm until the spanwise W mean velocity profile from a traverse across the z range at a constant $y = 4$ mm was anti-symmetric about the centerline.

Fig. 6 shows the magnitude of U_τ/U_{ref} ($\pm 3\%$ uncertain) that was determined by the viscous sublayer data as mentioned earlier. The results show a maximum at the centerline that is due to the strong downwash of the trailing vortices. On each side where data are available, there is an almost symmetric oscillation for $|x|/H <$

0.81 . Thus, the other oscillations appear credible. A local minimum occurs at $z/H = -1.9$, where low velocity flow is observed from the oil flow. For the 2D flow without the bump, $U_\tau/U_{ref} = 0.04$, so the 3D flow has lower wall stresses across the span except near the centerline.

Figs. 7 and 8 show the mean streamwise U and W velocity components normalized in wall variables on the local U_τ from Fig. 6, while Figs. 9–12 show turbulence quantities. Since there is no law of the wall for mean 3D flows, collapse of the U^+ results onto a single line is not expected. Near the centerline there are much higher U^+ values because of the downwash of the trailing vortices,

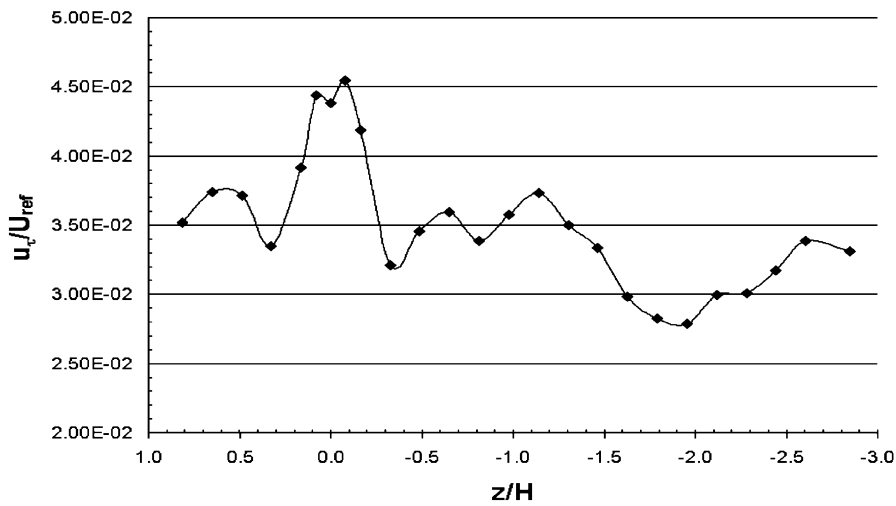


Fig. 6. Variation of U_τ/U_{ref} across the flow at $x/H = 3.69$.

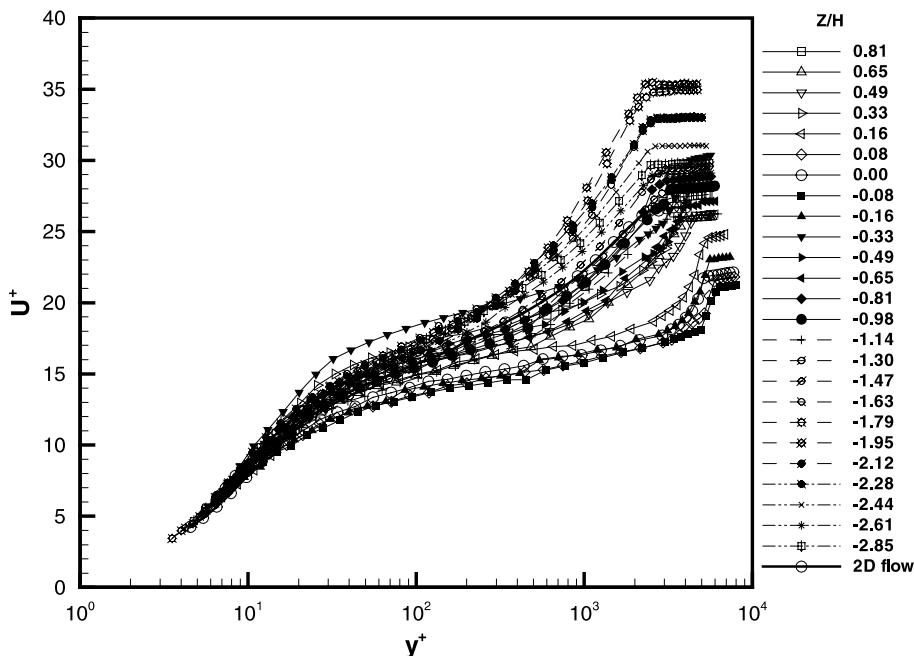


Fig. 7. Streamwise mean velocity profiles at $x/H = 3.69$.

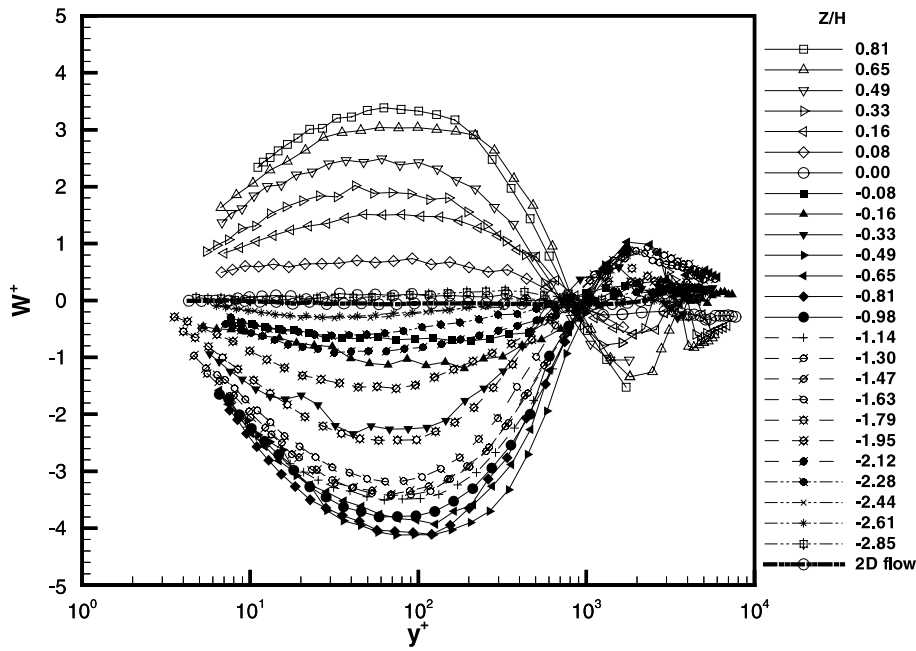


Fig. 8. Spanwise mean velocity profiles at $x/H = 3.69$.

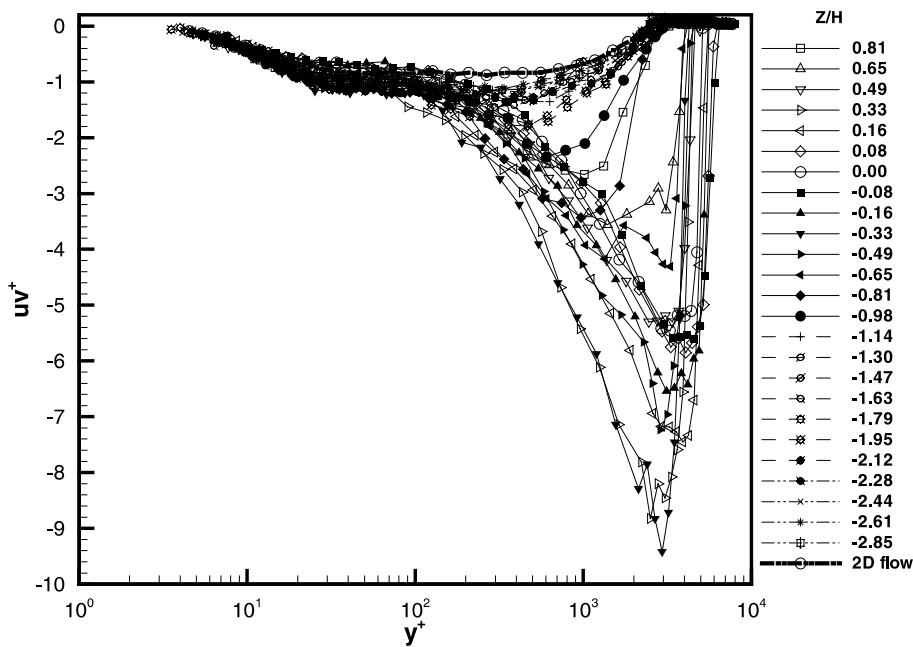


Fig. 9. Streamwise Reynolds shearing stress at $x/H = 3.69$.

while the flow outside the vortex pair is much slower. In this plot, most of the apparent asymmetry between data on opposite sides of the centerline is due to the different U_z used to form U^+ . The W^+ is about zero at $y^+ \approx 900$ for all z/H , which is the apparent height of the vortex centers. The $\partial W/\partial y \approx 0$ and the flow gradient angle ($\tan^{-1}(\partial W/\partial y)/(\partial U/\partial y)$) are about zero for $70 < y^+ < 90$ for all z/H , so the streamwise vorticity nearer the wall

is of opposite sense to that further away. Although not all outer region profiles are shown, they indicate good symmetry on opposite sides of the centerline within experimental uncertainties.

The streamwise Reynolds shearing stress $-\overline{uv}$ (Fig. 9) has similar profiles between the wall and the height of $70 < y^+ < 80$ at all z/H . The shearing stress angle $\tan^{-1}(-\overline{vw}/-\overline{uv})$ (Fig. 10) is also zero within $\pm 5^\circ$ at

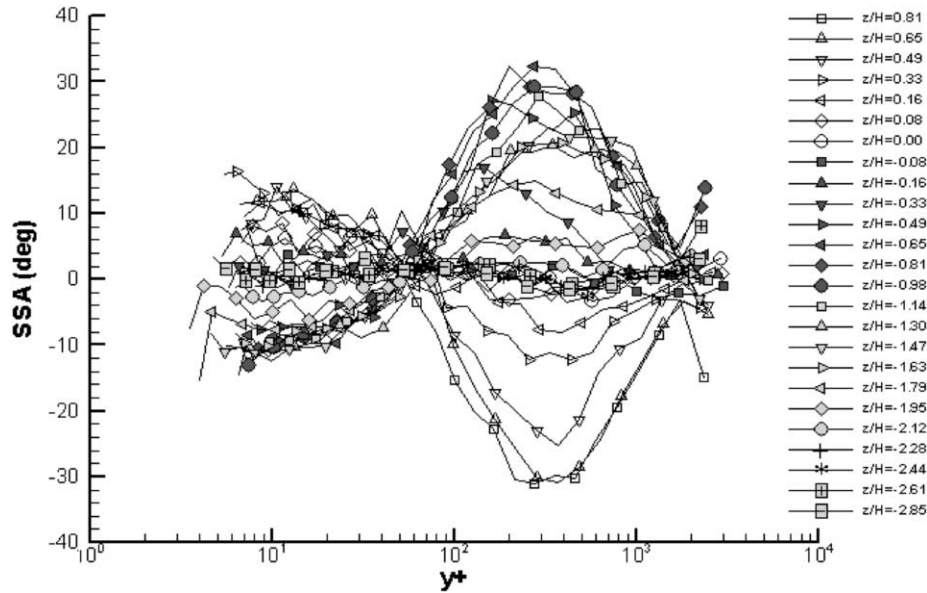


Fig. 10. Shear-stress angle at $x/H = 3.69$.

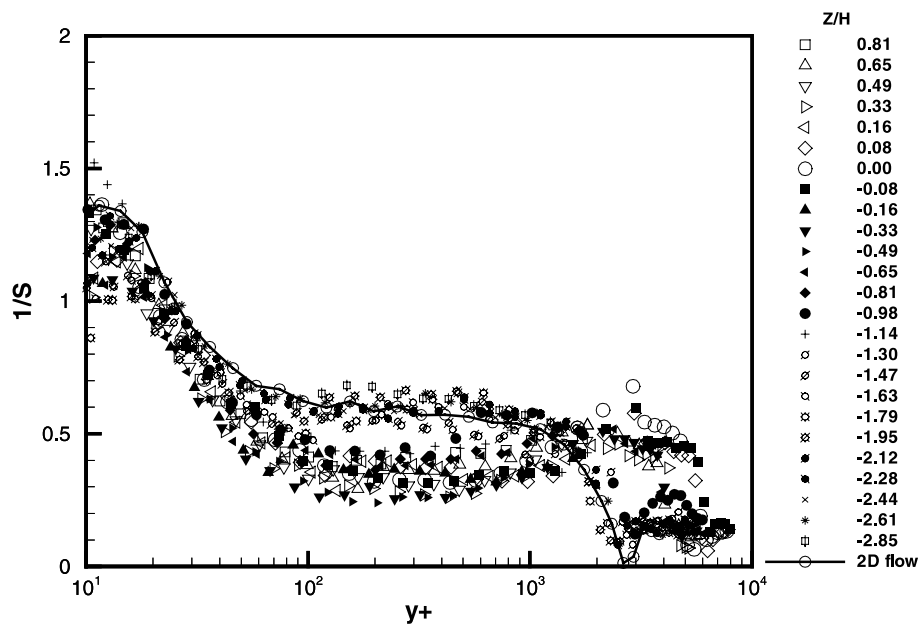


Fig. 11. $S = [(-\overline{uw})^2 + (-\overline{vw})^2]^{0.5} / \overline{v^2}$ versus y^+ at $X/H = 3.69$.

$y^+ \approx 60$ for all z/H . The spanwise Reynolds shearing stress $-\overline{vw}$ is of opposite sign above and below this region.

The parameter $1/S = [(-\overline{uw})^2 + (-\overline{vw})^2]^{0.5} / \overline{v^2}$ shown in Fig. 11 also has similarity across the flow at nearly all z/H locations for $y^+ < 40$. For locations further from the centerline than the mean vortex, the level of $1/S$ for $100 < y^+ < 1000$ is close to that for the 2D flow and is about the same level as observed in 3D flows without embedded vortices. Near the centerline where the downwash effects are large a different similarity is observed. These two similarities in these two regions are

much better than the similarity of the R_{uv} correlation coefficient across the flow, which is not shown here. This indicates that the relationship between the $\overline{v^2}$ and the shearing stress is stronger than the relationship between the u' and the v' that appear in the R_{uv} correlation coefficient.

The streamwise normal stress $\overline{u^2}$ (not shown here) also has similar shaped profiles out to about $y^+ \approx 70$ or so, even though the local near-wall maximum $\overline{u^2}$ levels near $15 < y^+ < 30$ increase around the centerline of the flow and their location is at a higher y^+ than at the large z/H locations.

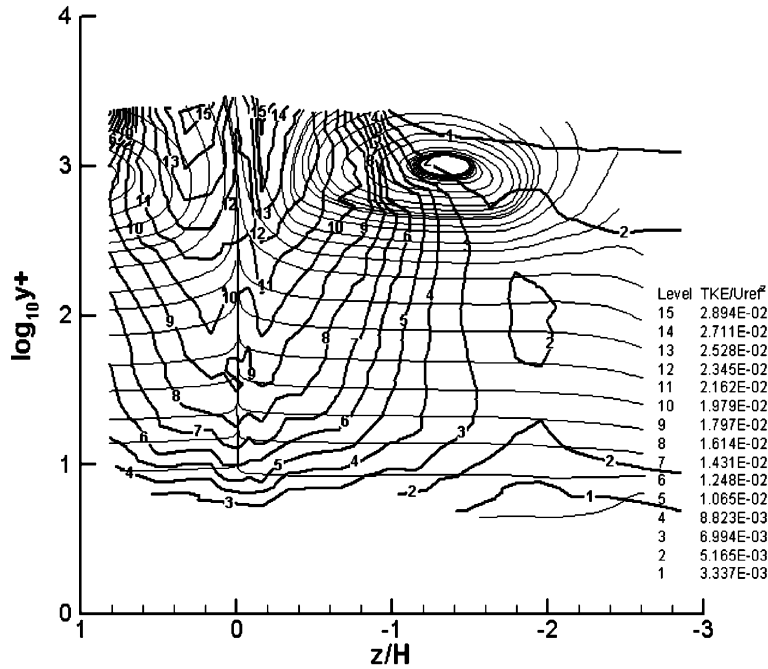


Fig. 12. Turbulence kinetic energy levels (TKE/U_{ref}^2) in the measurement plane (dark lines). Secondary flow (V, W) lines shown as thin lines.

These data show that the wall and the turbulence production near the wall dominate the flow structure near the wall for $y^+ < 90$. It is also noteworthy to mention that for $|z|/H > 1.6$, all of the Reynolds stresses and triple products have similar profiles. Away from the wall in the center, the large turbulence levels (Fig. 12, $TKE = \overline{q^2}/2 = (\overline{u^2} + \overline{v^2} + \overline{w^2})/2$) are produced by the strong streamwise vortices.

It is also interesting that the correlation coefficient R_{uw} is unusually low $|R_{uw}| < 0.25$ in the region of $0 <$

$|z|/H < 1.2$ and $30 < y^+ < 500$, while it is above 0.35 for the outer region and for a 2D flow. It must be due to the larger $\overline{u^2}$ present there, since the $-\overline{uw}$ values do not appear to be large in this zone. The R_{uw} for the large $|z|/H$ values behave more like those for the undisturbed 2D case.

All triple products were also measured (Long, 2002). Fig. 13 shows the transport velocity vectors $(V_{qv}\vec{j} + V_{qw}\vec{k})/U_{ref} = (\overline{vq^2}\vec{j} + \overline{wq^2}\vec{k})/\overline{q^2}U_{ref}$ derived from the triple products. These vectors show the large transport of

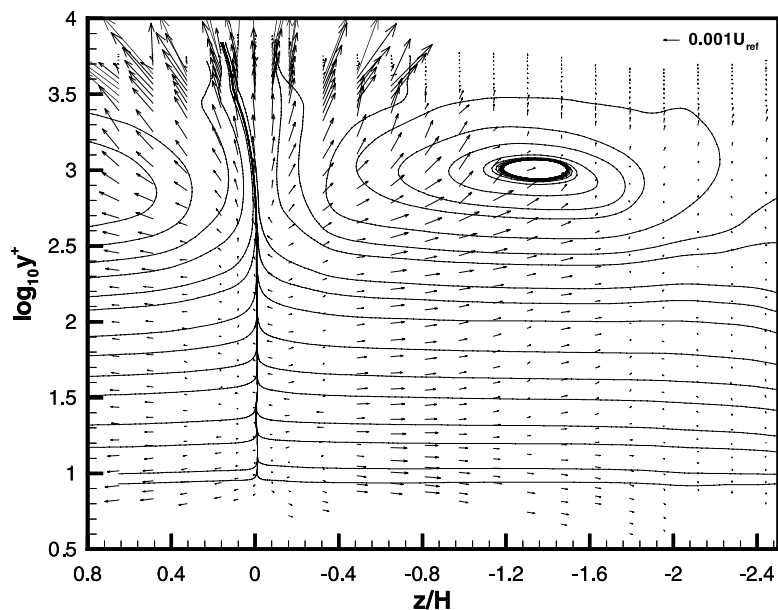


Fig. 13. Vector plot for the mean transport velocity of TKE in y - z plane, normalized by U_{ref} , and secondary flow streamlines.

TKE away from the centerline where it has the greatest values. Again the region $|z|/H > 1.6$ shows low values of the triple products and the transport velocity.

A spectrum analysis was done of the high intensity spanwise velocity fluctuation w data at $z/H = 0$ and $y^+ = 740$. Although the LDV coincident data rate was about 200, low frequencies could be examined. The spectrum has a peak at $fH/U_{\text{ref}} \approx 0.003$ and a f^{-1} slope for $0.005 < fH/U_{\text{ref}} < 0.1$. These results suggest low frequency large amplitude spanwise meandering of the large shed vortex structures, such as suggested by Ishihara et al. (1999).

8. Discussion and conclusions

Surface mean pressures, oil-flow visualizations, and three-velocity-component laser-Doppler velocimeter measurements were presented for a turbulent boundary layer over an axisymmetric hill. The mean flow appears to be closely symmetric about the centerline. Complex vortical separations occur on the leeside and merge into two large streamwise vortices downstream. At $x/H = 3.69$, the near-wall flow ($y^+ < 90$) is dominated by the wall, while the vortices in the outer region produce large turbulence levels near the centerline and appear to have low frequency motions that contribute to turbulent diffusion.

The LDV- and oil-flow results are clearly consistent with one another. The flow along the streamwise centerline at $x/H = 3.69$ is a downwashing reattachment flow and only one mean vortex exists on each side of the centerline, which is qualitatively the same as the pitot-static tube measurement results reported by Willits and Boger (1999) for the same shape bump with the same $\delta/H = 1/2$. These two independent sets of results do not support the unpublished computational results for this geometry and flow from several different research groups using several two-equation turbulence models. The $k-\omega$ model has been observed to improve calculations for mean 2D separating flows (Simpson, 1996). However, when used to compute this bump flow, a separation is calculated along the centerline and two streamwise mean vortices are produced on each side of the centerline. These current LDV results indicate that

this $k-\omega$ turbulence model does not capture the important physics of this separating vortical 3D flow. The diffusion and merger of the leeside separations into the observed downstream structure needs to be better modeled. The low frequency chaotic meandering of the shed vortex structure probably needs to be included since this would increase the diffusion. More detailed three-velocity-component LDV measurements closer to the wall and around the locations of the separations are needed for greater understanding and improvements to future models.

Acknowledgements

This work was supported by the US Office of Naval Research under N00014-99-1-0228, Dr. L.P. Purtell, Program Manager. The tabulated data are located at <http://www.aoe.vt.edu/aoe/faculty/rogfac.html>.

References

- Devenport, W.J., Simpson, R.L., 1990. Time dependent and time averaged turbulence structure near the nose of a wing-body junction. *J. Fluid Mech.* 210, 23–55.
- Hunt, J.C.R., Abell, C.J., Peterka, J.A., Woo, H., 1977. Kinematical studies of the flows around free or surface-mounted obstacles; applying topology to flow visualization. *J. Fluid Mech.* 86 (1), 179–200.
- Ishihara, T., Hibi, K., Oikawa, S., 1999. A wind tunnel study of turbulent flow over a three-dimensional steep hill. *J. Wind Eng. Indus. Aerodyn.* 83, 95–107.
- Long, C.H., 2002. A study of vortical separation from symmetric bumps. MS Thesis, Aerospace and Ocean Engineering, VPI&SU, in progress.
- Ölçmen, M.S., Simpson, R.L., 1995. A 5-velocity-component laser-Doppler velocimeter for measurements of a three-dimensional turbulent boundary layer. *Meas. Sci. Tech.* 6, 702–716.
- Ölçmen, M.S., Simpson, R.L., George, J., 2001. Some Reynolds number effects on two- and three-dimensional turbulent boundary layers. *Exp. Fluids* 31, 219–228.
- Simpson, R.L., 1996. Aspects of turbulent boundary-layer separation. *Prog. Aerospace Sci.* 32, 457–521.
- Willits, S.M., Boger, D.A., 1999. Measured and predicted flows behind a protuberance mounted on a flat plate. Applied Research Laboratory Report, Penn State Univ., State College, PA, August 30.